CJC Chinese Journal of Chemistry 中国化学 - An International Journal

For submission: https://wiley.atyponrex.com/journal/CJOC
For published articles: https://onlinelibrary.wiley.com/journal/16147065

Concise Report

Cite this paper: *Chin. J. Chem.* **2025**, *43*, 3193—3198. **DOI: 10.1002/cjoc.70219**

Interplay of Crystal Structures, Thermal Properties, and Magnetism in Zero-Dimensional Hybrid Transition Metal Bromides

Sinuo Li,[a] Richard J. Harrison,[a] Wei Li,[b] and Michael A. Carpenter*[,a]

[a] *Department of Earth Sciences, University of Cambridge, Downing Street, Cambridge, Cambridgeshire CB2 3EQ, United Kingdom*
[b] *School of Materials Science and Engineering, Nankai University, Tianjin 300350, China*

Keywords

0D hybrid metal halides | Transition metal | Packing structure | Phase transition | Magnetism

Comprehensive Summary

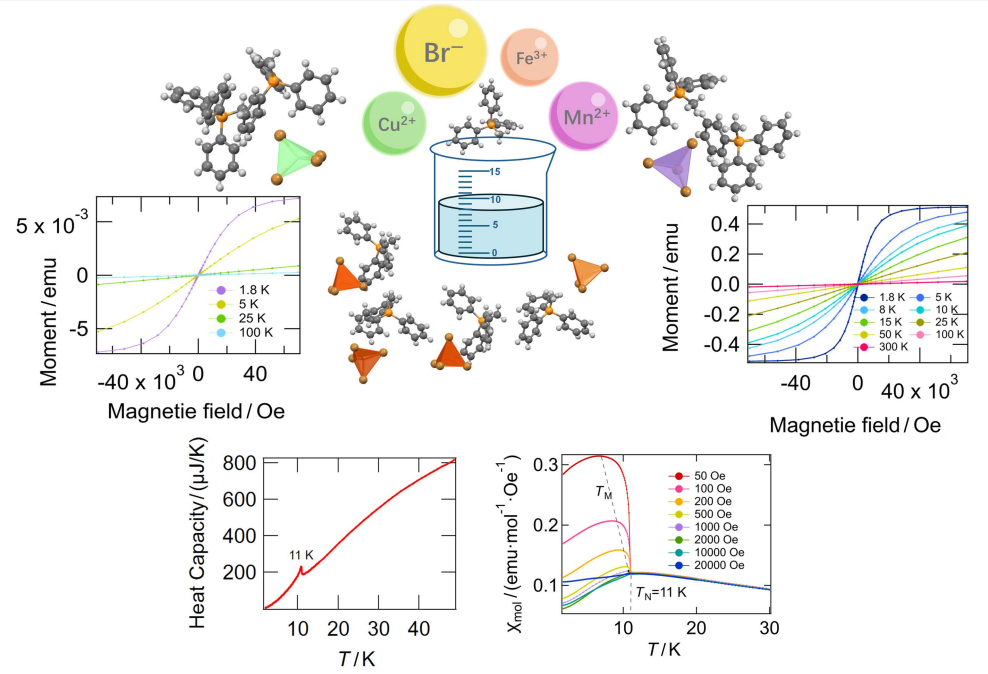

This paper investigates the structure-property relationships of three zero dimensional (0D) organic-inorganic hybrid metal halides, focusing on the influence of metal cations on their thermal and magnetic properties. Three transition metal bromides—$MnBr_2$, $FeBr_3$, and $CuBr_2$—were selected to coordinate with a large organic ion, $(C_6H_5)_3PCH_3^+$, to form 0D hybrid structures. By maintaining the organic component constant and varying the metal centres, we explore how the metal cation affects the structural characteristics, thermal and magnetic properties using differential scanning calorimetry (DSC), heat capacity measurements and magnetic measurements. The results indicate the influence of metal cations on packing styles and intermolecular interactions of 0D hybrid metal halides, which contribute to the different thermal and magnetic behaviours. Through varying metal cation, it is possible to tune properties by affecting structural characteristics, which could be significant for designing and optimizing devices and applications. In particular, the Fe-phase is multiferroic below 11 K, *i.e.*, ferroelastic, ferroelectric and weakly ferromagnetic.

*E-mail: mc43@cam.ac.uk

Background and Originality Content

Organic-inorganic hybrid materials are currently a subject of great interest in the materials science community because of their excellent properties and abundant structures.[1] The incorporation of organic molecules endows hybrid materials with diverse structures, for example, three-dimensional (3D) frameworks, two-dimensional (2D) layers, one-dimensional (1D) chains or zero-dimensional (0D) packing structures.[2] Among these, 0D hybrid metal halides have attracted increasing attention due to simple synthesis and superior properties, such as wide bandgaps, high photoluminescence quantum yield (PLQY), large Stokes shifts, broad emission spectra, long luminescence lifetimes[3] and low antiferromagnetic ordering temperatures.[4] Compared with other dimensional hybrids, 0D hybrids allow more opportunities for micromovements, such as rotation, distortion,[5] vibration,[6] as a result of the absence of restrictive framework structures. These dynamic movements within 0D hybrids enhance their ability to respond to external stimuli, for example, temperature,[7] stress,[8] X ray,[9] electric field,[10] thereby contributing to their diverse properties.

In the structure of 0D hybrids, metal cations significantly influence the electronic, optical, and magnetic properties. They play a crucial role in the coordination environment and structural properties, while also governing the charge transport and electronic band structure.[11] The d-orbital configuration and coordination geometry can introduce unique electronic states and tuneable properties, such as luminescence[12] and magnetic behaviour,[13] which are difficult to achieve by changing the halogen or organic component alone. Therefore, investigating the role of different metals allows for more precise control over the material's properties, enabling the design of hybrid materials with tailored functionalities for specific applications.

To date, the majority of 0D hybrid material research has focused on their photoelectric and piezoelectric applications,[1c,14] with much less attention given to the fundamental understanding of the mechanisms that govern their behaviour. A deeper exploration of structure-property relation is crucial for unveiling the intrinsic transitions.

In this paper, we investigate the influence of metal components on the properties of 0D hybrid metal halides. We use three transition metal bromides—$MnBr_2$, $FeBr_3$, and $CuBr_2$—to coordinate with the large-sized organic ion $(C_6H_5)_3PCH_3^+$ forming 0D hybrid structures. By keeping the organic component constant and systematically varying the metal components, we unravel how the metal cation influences the structural, thermal and magnetic properties.

Results and Discussion

Structures

$(C_{19}H_{18}P)_2MnBr_4$ crystallizes in monoclinic space group $P2_1$, with cell parameters a = 9.7399(1) Å, b = 12.3887(1) Å, c = 16.4947(1) Å and β = 104.9970(1)° at 100 K (Table S2).[8] As shown in Figure 1(a), it adopts a zero-dimensional packing structure, and each unit cell contains two asymmetric units. Each asymmetric unit consists of two organic molecular cations $[C_{19}H_{18}P]^+$ and one $[MnBr_4]^{2-}$ tetrahedron, maintaining charge balance. $[C_{19}H_{18}P]^+$ organic molecular cations interact with $[MnBr_4]^{2-}$ tetrahedra through electrostatic forces. Inside the tetrahedral unit, the Br–Mn–Br angles range from 107.34° to 112.44°, and the Br–Mn bond lengths range from 2.49 to 2.53 Å.

$(C_{19}H_{18}P)_2CuBr_4$ crystallizes in monoclinic space group Cc, with cell parameters a = 11.910(2) Å, b = 14.889(3) Å, c = 20.904(4) Å and β = 92.73(3)° at 100 K (Table S2).[15] As shown in Figure 1(b), it has a 0D structure with four asymmetric units in the unit cell. Each asymmetric unit consists of two organic molecular cations $[C_{19}H_{18}P]^+$ and one $[CuBr_4]^{2-}$ tetrahedron. Compared with $(C_{19}H_{18}P)_2MnBr_4$ and $(C_{19}H_{18}P)FeBr_4$, the $[CuBr_4]^{2-}$ tetrahedra are highly distorted due to the Jahn-Teller effect (Figure 1e), with Br–Cu–Br angles ranging from 96.76° to 137.96°, and Br–Cu bond lengths ranging from 2.35 to 2.42 Å (100 K). A second monoclinic structure, also with space group Cc (Table S2), has been observed at 373 K (a = 9.0171(3) Å, b = 25.1547(1) Å, c = 17.6036(6) Å and β = 102.705(3)°). It also contains highly distorted $CuBr_4$ tetrahedra. This distortion becomes more pronounced with increasing temperature (Table S9). Compared with other 0D copper(II) hybrids of similar structures, this material exhibits the largest distortion (Table S9).

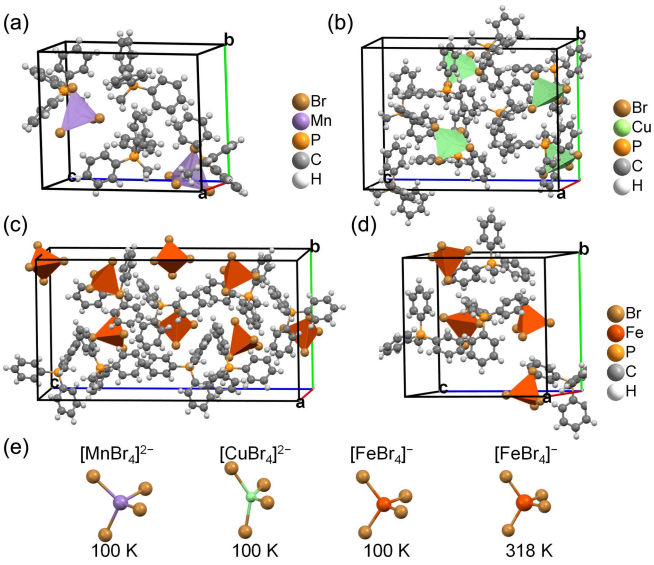

Figure 1 Single crystal structures in the unit cell.(a) $(C_{19}H_{18}P)_2MnBr_4$ at 100 K.[8] (b) $(C_{19}H_{18}P)_2CuBr_4$ at 100 K.[15] (c) $(C_{19}H_{18}P)FeBr_4$ at 100 K. (d) $(C_{19}H_{18}P)FeBr_4$ at 318 K. (e) Ball-stick structures of $[MnBr_4]^{2-}$, $[CuBr_4]^{2-}$, $[FeBr_4]^-$ tetrahedra at 100 K and $[FeBr_4]^-$ tetrahedron at 318 K.

$(C_{19}H_{18}P)FeBr_4$ crystallizes at room temperature in the *ortho*-rhombic space group $P2_12_12_1$ (Table 1 and S1). At 100 K and 150 K the structure is in the monoclinic space group $P2_1$ (Table 1 and S1). $(C_{19}H_{18}P)FeBr_4$ adopts 0D structures, as shown in Figures 1c and 1d. The unit cell of the monoclinic form ($P2_1$) contains two asymmetric units including eight organic molecular cations, $[C_{19}H_{18}P]^+$, and eight inorganic anions $[FeBr_4]^-$. There are four asymmetric units per unit cell of the $P2_12_12_1$ structure, each containing one cation and one anion (Figure 1d). In both structures the tetrahedra are distorted, with Br–Fe–Br angles in the range 107.57°–112.80° ($P2_1$, 100 K) or 105.58°–115.77° ($P2_12_12_1$, 318 K) and Br–Fe bond lengths in the range 2.3225–2.3478 Å ($P2_1$) or 2.3014–2.3203 Å ($P2_12_12_1$). The lattice parameters of the $P2_1$ structure have double the c-repeat of the $P2_12_12_1$ structure (Table 1). There is a group/subgroup relationship between the two space groups such that a phase transition $P2_12_12_1$–$P2_1$ at some temperature between 300 and 150 K would be improper ferroelastic and improper ferroelectric. The presence of ferroelastic twinning has been confirmed by split reflections in a diffraction pattern collected at 100 K (Figure S1). The active representation for the transition is Z_1 of space group $P2_12_12_1$.[16]

The principal differences between the $P2_1$ (Figure 1c) and the $P2_12_12_1$ (Figure 1d) structures are the orientation and slight distortions of the tetrahedra. The shortest Fe–Fe distances between $[FeBr_4]^-$ tetrahedra are 7.627 Å ($P2_1$) and 7.809 Å ($P2_12_12_1$), which are the nearest distances among the three hybrid compounds considered here, indicating that $(C_{19}H_{18}P)FeBr_4$ has the closest packed arrangement (Table 2). This close packing influences structural, thermal, and magnetic properties, potentially making it distinct from the other samples.

Table 1 Space group and lattice parameters of $(C_{19}H_{18}P)FeBr_4$, as determined by single crystal X-ray diffraction at three different temperatures.

Parameters	100 K	150 K	318 K
Space group	$P2_1$	$P2_1$	$P2_12_12_1$
a/Å	10.90670(10)	10.94030(10)	11.1804(2)
b/Å	14.9007(2)	14.9449(2)	14.0599(3)
c/Å	27.8288(3)	27.8958(3)	15.1045(3)
α/(°)	90	90	90
β/(°)	91.1930(10)	91.1490(10)	90
γ/(°)	90	90	90
Volume/Å^3	4521.68(9)	4560.09(9)	2374.36(8)

Thermal properties

Heat flow and heat capacity measurements have revealed the temperatures of phase transitions and melting in the three compounds (Figure 2). The only anomaly present in data for $(C_{19}H_{18}P)_2MnBr_4$ indicates melting at ~451 K during heating and a glass transition at ~320 K during cooling (Figure 2a). Separate data (unpublished) showed anomalies in dielectric properties near 250 K, but heat capacity data between 240 and 310 K (Figure S2b) do not provide overt evidence that this could be due to a discrete phase transition.

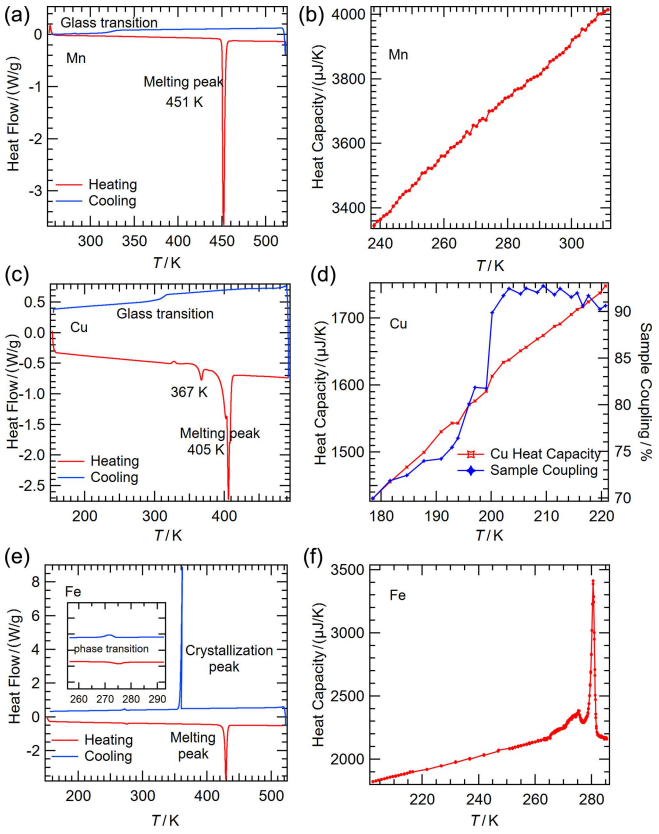

Figure 2 Thermal properties. Heat flow (a) and heat capacity (b) of $(C_{19}H_{18}P)_2MnBr_4$. Heat flow (c) and heat capacity (d) of $(C_{19}H_{18}P)_2CuBr_4$. Heat flow (e) and heat capacity (f) of $(C_{19}H_{18}P)FeBr_4$.

$(C_{19}H_{18}P)_2CuBr_4$ melted at ~405 K during heating and underwent a glass transition at ~310 K during cooling (Figure 2c). An additional anomaly was observed at 367 K during heating (Figure 2c) and is attributed to a reconstructive transition between the two structures with *Cc* symmetry. A single crystal of $(C_{19}H_{18}P)_2CuBr_4$ emerged as a powder after cycling to low temperatures and similar disintegration occurred in attempts to measure other physical properties at low temperatures. The steep change in thermal conduction between the sample and the sample platform of the PPMS instrument at ~200 K evident in Figure 2d (right axis), suggests this as the temperature at which the crystal broke up. An abrupt change in volume or shear strain might be responsible but, if it was due to a phase transition, it may have been smeared over some temperature interval as there is no overt evidence of a discrete anomaly in the heat capacity (Figure 2d, left axis).

$(C_{19}H_{18}P)FeBr_4$ melted at ~430 K during heating, but the sharp DSC peak at ~360 K indicates that it recrystallised during cooling, rather than undergoing a glass transition. The difference between glass formation and crystallisation may be due to looser packing in the Cu and Mn phases which allows for increased molecular mobility and weaker intermolecular interactions, slowing down the rate of crystallization.[14c] The $P2_1$-$P2_12_12_1$ transition is evident as a small anomaly in the heat flow data at 275 K during heating and at 271 K during cooling (Figure 2e). A sharp peak in heat capacity at ~280 K indicates that it is first order in character, but two shoulder peaks at ~267 K and 274 K suggest that there were additional precursor changes in structure.

Magnetic properties

Mn^{2+}, which has a half-filled d-shell electron structure, is the only component creating magnetic moments in $(C_{19}H_{18}P)_2MnBr_4$. As shown in Figure 3(a), the (inverse) susceptibility validates $(C_{19}H_{18}P)_2MnBr_4$ as paramagnetic, with the inverse susceptibility crossing zero at 0 K. Through fitting the inverse susceptibility to the Curie Weiss law for paramagnetism, $x = C/T$, the calculated Curie constant C is 4.79(5), and the effective magnetic moment (μ_{eff}) is 6.19(3) μ_B, which correlates with the high spin state (μ_{eff} = 5.92μ_B). The five d electrons in Mn^{2+} are in the high spin state and the total angular momentum quantum number (J) is 5/2. According to the Brillouin function for a paramagnet,[17] $x = Jg\mu_BB/k_BT$, where g is the g-factor, μ_B is the Bohr magnon, B is the applied magnetic field, k_B is the Boltzmann constant, and T is the temperature (the temperature for observation and calculation is 1.8 K). Taking the g-factor as −2, we can obtain x. Appending this trace to the Brillouin function curve with J = 5/2 to compare the observed result with theoretical curve, shows a perfect fit in Figure 3e, confirming $(C_{19}H_{18}P)_2MnBr_4$ to be a standard paramagnet.

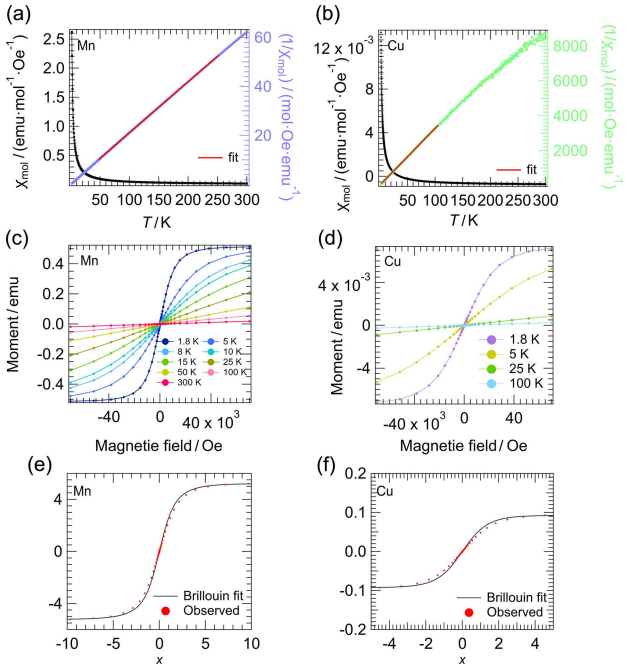

Figure 3 Magnetic measurement results. (a) Susceptibility and inverse susceptibility of $(C_{19}H_{18}P)_2MnBr_4$. (b) Susceptibility and inverse susceptibility of $(C_{19}H_{18}P)_2CuBr_4$. (c) Magnetization of $(C_{19}H_{18}P)_2MnBr_4$ with respect to the applied field at different temperatures. (d) Magnetization of $(C_{19}H_{18}P)_2CuBr_4$ with respect to the applied field at different temperatures. (e) Brillouin fit for $(C_{19}H_{18}P)_2MnBr_4$. (f) Brillouin fit for $(C_{19}H_{18}P)_2CuBr_4$.

Table 2 Crystallographic and electronic information at 100 K.

	$(C_{19}H_{18}P)_2MnBr_4$[a]	$(C_{19}H_{18}P)FeBr_4$	$(C_{19}H_{18}P)_2CuBr_4$[b]
Metal centre distance/Å	12.16	7.63	9.53
Number of organic molecular cations in unit cell	4	8	8
Number of tetrahedra in unit cell	2	8	4
Cell volume/Å^3	1922.54	4521.68	3702.66
d orbital structure	$3d^5$	$3d^5$	$3d^9$
Spin state	High spin	High spin	Low spin
Jahn-Teller effect	no	no	strong

[a] Data of $(C_{19}H_{18}P)_2MnBr_4$ at 100 K is from Wei Li's report.[8] [b] Data of $(C_{19}H_{18}P)_2CuBr_4$ at 100 K is from Ramamoorthy Boomishankar's report.[15]

ZFC and FC magnetic data in Figure S2 indicate that $(C_{19}H_{18}P)_2MnBr_4$ does not exhibit spin splitting or significant changes in magnetic state between the two cooling methods. The pattern of magnetization in Figure 3c follows the Curie law. Without magnetic field, the moment was weakly coupled and randomly aligned due to thermal agitation. As shown in Figure 3c the magnetization at 1.8 K reached saturation in a 5 Tesla field.

In Cu^{2+} there are nine electrons in d-orbitals, with eight paired and one unpaired. Under applied field, the unpaired electron produces a small magnitude of magnetisation. Magnetic data for $(C_{19}H_{18}P)_2CuBr_4$, after subtraction of the background signal from the sample holder (Figure S3), are shown in Figures 3b and 3d and indicate paramagnetic behaviour. The Curie constant for $(C_{19}H_{18}P)_2CuBr_4$ is 0.030(6). Figure 3f shows the Brillouin fit for $(C_{19}H_{18}P)_2CuBr_4$, also validating its paramagnetic behaviour.

Figures 4, S4 and S5 show the magnetic properties of $(C_{19}H_{18}P)FeBr_4$ at different temperatures, as measured with the applied field aligned parallel to the crystallographic *c*-axis. Variations of the susceptibility, χ, match those of a paramagnetic phase from room temperature down to an antiferromagnetic ordering transition at T_N = 11 K (Figures 4a and S4). A peak in the heat capacity at 11 K (Figure 4c) confirms the transition. The inverse susceptibility in the range 100–300 K fits the Curie-Weiss law (Figure 4b), $\chi^{-1} = (T-\vartheta)/C$,[17] with C = 4.998(5), ϑ = −19.05 K and μ_{eff} = 6.32(3)μ_B, consistent with Fe^{3+} ions being in the high spin state (S = 5/2).The negative ϑ is often observed in antiferromagnetic materials above their Néel temperature, which suggests the presence of antiferroelectric interactions. An additional anomaly in the susceptibility was found below T_N and varied with the strength of the applied field (Figures 4a,b and S4). As the external field decreased, the sharp peak at T_M increased in magnitude and became pronounced, consistent with a ferromagnetic component due to spin canting. In this case, the spins were not perfectly antiparallel, with canting by only a fraction of degree, resulting in the rise in susceptibility.

Magnetization as a function of field for $(C_{19}H_{18}P)FeBr_4$ includes inflections at 1.8 K and 5 K (Figures 4d, S5). According to a previous report, $(PEA)_2MnCl_4$[18] shows a similar inflection when the field is out-of-plane, which was interpreted in terms of spin flop behaviour. However, there are not enough data for the susceptibility under different orientations of the field (*e.g.* in-plane and out-of-plane) for this to be confirmed in the present case. Figure S6 shows narrow hysteresis loops at 1.8 K and 5 K under small applied field (−5000 Oe to 5000 Oe). This also agrees with weak ferromagnetism caused by spin canting.

The choice of three transition metals for the present study resulted in different interactions between the metal bromide tetrahedra, and in varied packing structures, which subsequently influenced the dynamics within the system (Table 2). Mn^{2+} ions in $(C_{19}H_{18}P)_2MnBr_4$ are weakly interacting due to the relatively large distance between metal centres, presenting a very loose packing state. The same applies to Cu^{2+} in $(C_{19}H_{18}P)_2CuBr_4$. By way of contrast, $(C_{19}H_{18}P)FeBr_4$ exhibits the tightest structure, with the shortest distance between metal centres. The packing style determines whether there is weaker or stronger interaction between metal cations and whether there is more or less space for rotational displacements of the organic components. These structural factors then influence the crystallization, phase transitions, and magnetic behaviour of each phase. Both Mn^{2+} and Fe^{3+} have five electrons in their d orbital and remain in a high-spin state. Cu^{2+} has one unpaired electron and the $[CuBr_4]^{2-}$ tetrahedra are distorted due to a strong Jahn-Teller effect. $(C_{19}H_{18}P)FeBr_4$ is in principle multiferroic below 11 K in that it is expected to be ferroelectric, ferroelastic and weakly ferromagnetic.

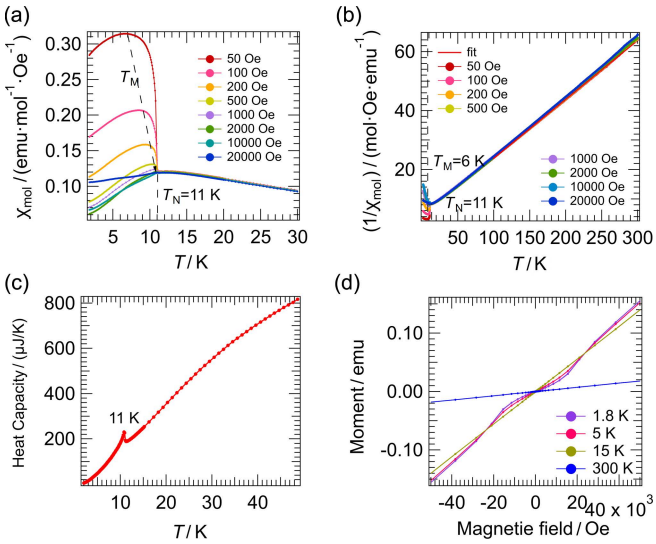

Figure 4 Magnetic and heat capacity results. (a) Zoomed in result for $(C_{19}H_{18}P)FeBr_4$ susceptibility. (b) Inverse susceptibility of $(C_{19}H_{18}P)FeBr_4$. (c) Low temperature heat capacity of $(C_{19}H_{18}P)FeBr_4$. (d) Zoomed in magnetization of $(C_{19}H_{18}P)FeBr_4$ with respect to applied field at different temperatures.

Conclusions

In this work, we have used heat flow, heat capacity and MPMS measurements to characterise similarities and differences between three 0D hybrid transition metal bromides. They display paramagnetism, antiferromagnetism, ferromagnetism due to spin canting, a potential spin-flop transition, a first order ferroelastic transition, a reconstructive transition between structures with the same space group, different crystallisation/glass transition behaviour and, in the case of the Cu phase, a strong Jahn-Teller effect. Single crystals of the Cu phase also have some structural change which are sufficient to cause them to break up into small pieces.

This phenomenologically rich diversity in just three compounds is shaped by the fact that the metal tetrahedra can rotate relatively freely in 0D structures. The three different metal cations contribute significantly to packing density, molecular flexibility and electronic interactions, which in turn impact the structural, thermal and magnetic properties. It must be expected that 0D hybrid transition metal organic compounds, more widely, represent a class of materials with the potential to display a wide range

of functional properties in bulk or as thin films that can be tuned or manipulated according to the choice of metal cation.

Experimental

Sample synthesis

$(C_{19}H_{18}P)_2MnBr_4$: 0.7144 g $C_{19}H_{18}PBr$ (2 mmol) was dissolved in ethanol (5 mL), then 0.2148 g $MnBr_2$ (1 mmol) was added. After ultrasonic agitation, 1.5 mL HBr was added to the transparent solution. Following a few days of evaporation at room temperature, transparent, bright green single crystals with dimensions of ~5 x 5 x 2 mm^3 were obtained.

$(C_{19}H_{18}P)FeBr_4$: 0.3572 g $C_{19}H_{18}PBr$ (1 mmol) was dissolved in 5 mL water, then 0.2956 g $FeBr_3$ (1 mmol) was added. Ultrasonic agitation was used to dissolve the powder. The solvent was evaporated at room temperature for several days. Dark brown single crystals with dimensions of ~2 × 1 × 1 mm^3 were obtained.

$(C_{19}H_{18}P)_2CuBr_4$: The same process as for the Fe and Mn samples was followed, with the exception that 0.7144 g $C_{19}H_{18}PBr$ (2 mmol) and 0.2234 g $CuBr_2$ (1 mmol) were added to 5 mL water. After several days of evaporation at room temperature, dark purple prismatic single crystals with dimensions of ~10 × 2 × 2 mm^3 were obtained.

Single crystal X-ray diffraction

Single crystal X-ray diffraction data were collected on a Rigaku XtaLAB MM007CCD diffractometer (Cu Kα λ = 1.54184 Å). ~0.05 mm sized single crystals of three samples were used. For $(C_{19}H_{18}P)_2MnBr_4$, structure at 100 K was measured and published.[8] For $(C_{19}H_{18}P)_2CuBr_4$, structures at 293 K and 373 K were measured and were deposited in the Cambridge Crystallo-graphic Data Centre (CCDC) under the reference number 2451467 (293 K) and 2453652 (373 K). For $(C_{19}H_{18}P)FeBr_4$, structures at 100 K, 150 K and 318 K were measured and were deposited in CCDC under the reference number 2430770 (100 K), 2209969 (150 K) and 2209981 (318 K). Liquid nitrogen was used to cooling the system. Data collection and structural refinement were carried out with Rigaku CrysAlisPro and Olex 2 software package.[19] The crystal data and structure refinement parameters are listed in Tables S1 and S2 of the Supporting Information.

Heat flow

Heat flow was measured using a TA DSC25 Differential Scanning Calorimeter. Sample powder was sealed in a Tzero Aluminum pan and measured under helium atmosphere. For $(C_{19}H_{18}P)_2MnBr_4$, 5 mg of powder was measured from 380 K to 460 K with the heating/cooling rates of 10 $K{\cdot}min^{-1}$. For $(C_{19}H_{18}P)_2CuBr_4$, 5.2 mg of powder was measured from 128 K to 548 K with heating/cooling rates of 20 $K{\cdot}min^{-1}$. For $(C_{19}H_{18}P)FeBr_4$, 5.3 mg of powder was measured from 128 K to 548 K with heating/cooling rates of 20 $K{\cdot}min^{-1}$.

Heat capacity

Heat capacity was measured using the heat capacity option in a Quantum Design Dynacool physical properties measurement system. Apiezon N grease was used to couple $(C_{19}H_{18}P)FeBr_4$ and $(C_{19}H_{18}P)_2CuBr_4$ to the heat capacity option stage; Apiezon H grease was used for $(C_{19}H_{18}P)_2MnBr_4$. The heat capacity for $(C_{19}H_{18}P)FeBr_4$ was measured from 2 K to 50 K, and from 202 K to 300 K. For $(C_{19}H_{18}P)_2CuBr_4$, the heat capacity was measured from 178 K to 220 K. For $(C_{19}H_{18}P)_2MnBr_4$, it was measured from 238 K to 311 K.

Magnetic property measurement system (MPMS)

Magnetic measurements were undertaken using a Quantum Design MPMS Squid magnetometer. A straw was used as the sample holder in this experiment. The sequence of measurement for the three samples involved zero field cool (ZFC), field cool (FC) and magnetization scans. For $(C_{19}H_{18}P)_2MnBr_4$ and $(C_{19}H_{18}P)_2CuBr_4$, the ZFC run involved cooling without field and then heating the sample in a field of 1000 Oe to measure susceptibility during heating. For $(C_{19}H_{18}P)FeBr_4$, the ZFC run involved cooling without field and then heating the sample in a field of 50 Oe, 100 Oe, 200 Oe, 500 Oe, 1000 Oe, 2000 Oe, 1 T and 2 T to measure susceptibility during heating. For $(C_{19}H_{18}P)_2MnBr_4$ and $(C_{19}H_{18}P)_2CuBr_4$, the FC run involved cooling in a 1000 Oe field and then heating in a field of 1000 Oe to measure susceptibility during heating. For $(C_{19}H_{18}P)FeBr_4$, the FC run involved cooling in a 1000 Oe field and then heating in a field of 50 Oe, 100 Oe, 200 Oe, 500 Oe, 1000 Oe, 2000 Oe, 1 T and 2 T to measure susceptibility during heating. The magnetization scans include setting target temperatures and then measuring magnetization from 0 T → 7 T → −7 T →0 T at each temperature. The direction of the applied field was parallel to the *c* axis of the three samples.

Supporting Information

The supporting information for this article is available on the WWW under https://doi.org/10.1002/cjoc.70219.

Acknowledgement

We would like to thank Dr. Rosa M. Danisi from University of Cambridge, Dr. Hang Qu and Laiyu Zhang from University of Liverpool for their generous assistance with crystallographic measurements and analysis.

References

[1] (a) Mao, L.; Chen, J.; Vishnoi, P.; Cheetham, A. K. The Renaissance of Functional Hybrid Transition-Metal Halides. *Acc. Mater. Res.* **2022**, *3*, 439–448; (b) Chen, Z.; Xue, J.; Wang, Z.; Lu, H. Magnetic Hybrid Transition Metal Halides. *Mater. Chem. Front.* **2024**, *8*, 210–227; (c) Vijayakanth, T.; Liptrot, D. J.; Gazit, E.; Boomishankar, R.; Bowen, C. R. Recent Advances in Organic and Organic–Inorganic Hybrid Materials for Piezoelectric Mechanical Energy Harvesting. *Adv. Funct. Mater.* **2022**, *32*, 2109492.

[2] Zhou, C.; Lin, H.; Lee, S.; Chaaban, M.; Ma, B. Organic–Inorganic Metal Halide Hybrids Beyond Perovskites. *Mater. Res. Lett.* **2018**, *6*, 552–569.

[3] (a) Cui, B. B.; Han, Y.; Huang, B.; Zhao, Y.; Wu, X.; Liu, L.; Cao, G.; Du, Q.; Liu, N.; Zou, W.; Sun, M.; Wang, L.; Liu, X.; Wang, J.; Zhou, H.; Chen, Q. Locally Collective Hydrogen Bonding Isolates Lead Octahedra for White Emission Improvement. *Nat. Commun.* **2019**, *10,* 5190.; (b) Fang, S.; Li, H.; Xie, Y.; Li, H.; Wang, Y.; Shi, Y. Zero-Dimensional Organic-Inorganic Hybrid Copper-Based Halides with Highly Efficient Orange-Red Emission. *Small* **2021**, *17*, 2103831; (c) Li, J.-L.; Sang, Y.-F.; Xu, L.-J.; Lu, H.-Y.; Wang, J.-Y.; Chen, Z.-N. Highly Efficient Light-Emitting Diodes Based on an Organic Antimony(III) Halide Hybrid. *Angew. Chem. Int. Ed.* **2022**, *61*, e202113450.

[4] Lee, K. W.; Lee, C. H.; Lee, C. E.; Kang, J. Magnetic Ordering in Two-Dimensional Heisenberg Antiferromagnets with Variable Interlayer Distances. *Phys. Rev. B* **2000**, *62*, 95.

[5] Pradhan, A.; Rana, R.; Rajaraman, G.; Pradhan, M.; Samal, S. L. $(C_3H_7NH_3)_4Bi_{1-x}Sb_xI_9$: 0D Hybrid Halide Perovskite-Like Compounds with Isolated Triiodide Units. *Dalton Trans.* **2024**, *53*, 13628–13637.

[6] Li, Y.; He, N.; Xu, B.; Dong, L.; Zhang, X.; Xu, J.; Gong, P.; Lin, Z. Synthesis, Structure, and Optical Properties of a 0D Hybrid Organic–Inorganic Metal Halide $(C_5N_2H_{14}Cl)GeCl_3$. *Inorg. Chem.* **2024**, *63*, 4412–4418.

[7] Liu, S.; Fang, X.; Lu, B.; Yan, D. Wide Range Zero-Thermal-Quenching Ultralong Phosphorescence from Zero-Dimensional Metal Halide Hybrids. *Nat. Commun.* **2020**, *11*, 4649.

[8] Yang, T.-Y.; Li, S.-N.; Chen, H.-S.; Li, Z.-Y.; Li, Z.-G.; Feng, R.; Gao, F.-F.;

Zhang, Y.; Liu, Y.-M.; Zhang, Y.; Liu, W.-W.; Li, W.; Bu, X.-H. Self-Recoverable Elastico Mechanoluminescence of a Hybrid Metal Halide Crystal. *Natl. Sci. Rev.* **2024**, *12*, nwae372.
[9] Li, B.; Xu, Y.; Zhang, X.; Han, K.; Jin, J.; Xia, Z. Zero-Dimensional Luminescent Metal Halide Hybrids Enabling Bulk Transparent Medium as Large-Area X-Ray Scintillators. *Adv. Opt. Mater.* **2022**, *10*, 2102793.
[10] Xu, L.-J.; Lee, S.; Lin, X.; Ledbetter, L.; Worku, M.; Lin, H.; Zhou, C.; Liu, H.; Plaviak, A.; Ma, B. Multicomponent Organic Metal Halide Hybrid with White Emissions. *Angew. Chem. Int. Ed.* **2020**, *59*, 14120–14123.
[11] Watcharatharapong, T.; Minakshi Sundaram, M.; Chakraborty, S.; Li, D.; Shafiullah, G. M.; Aughterson, R. D.; Ahuja, R. Effect of Transition Metal Cations on Stability Enhancement for Molybdate-Based Hybrid Supercapacitor. *ACS Appl. Mater. Interfaces* **2017**, *9*, 17977–17991.
[12] Jia, J.-H.; Zhang, D.-C.; Liang, D.; Wang, Q.; Wang, Z.-Q.; Zhang, L.; Lu, C.-Z. Luminescent Properties Variation Caused by Metal Cations Effect on the Deep Energy Levels in Cu(I) and Ag(I) Complexes. *Adv. Opt. Mater.* **2024**, *12*, 2303053.
[13] Asensio, Y.; Marras, S.; Spirito, D.; Gobbi, M.; Ipatov, M.; Casanova, F.; Mateo-Alonso, A.; Hueso, L. E.; Martín-García, B. Magnetic Properties of Layered Hybrid Organic-Inorganic Metal-Halide Perovskites: Transition Metal, Organic Cation and Perovskite Phase Effects. *Adv. Funct. Mater.* **2022**, *32*, 2207988.
[14] (a) Zhou, C.; Lin, H.; He, Q.; Xu, L.; Worku, M.; Chaaban, M.; Lee, S.; Shi, X.; Du, M.-H.; Ma, B. Low Dimensional Metal Halide Perovskites and Hybrids. *Mater. Sci. Eng. R Rep.* **2019**, *137*, 38–65; (b) Han, Y.; Yue, S.; Cui, B.-B. Low-Dimensional Metal Halide Perovskite Crystal Materials: Structure Strategies and Luminescence Applications. *Adv. Sci.* **2021**, *8*, 2004805; (c) Li, B.; Wang, Y.; Xu, Y.; Xia, Z. Emerging 0D Hybrid Metal Halide Luminescent Glasses. *Adv. Sci.* **2025**, *37*, 2415483; (d) Li, M.; Xia, Z. Recent Progress of Zero-Dimensional Luminescent Metal Halides. *Chem. Soc. Rev.* **2021**, *50*, 2626–2662.
[15] Sahoo, S.; Vijayakanth, T.; Kothavade, P.; Dixit, P.; Zaręba, J. K.; Shanmuganathan, K.; Boomishankar, R. Ferroelectricity and Piezoelectric Energy Harvesting of Hybrid A_2BX_4-Type Halogenocuprates Stabilized by Phosphonium Cations. *ACS Mater. Au* **2022**, *2*, 124–131.
[16] Stokes, H. T.; Hatch, D. M. *Isotropy Subgroups of the 230 Crystallographic Space Groups,* World Scientific, **1989**, p. 624.
[17] Crangle, J. *The Magnetic Properties of Solids,* Edward Arnold, London, **1977**, p. 27, pp. 64–66.
[18] (a) Septiany, L.; Tulip, D.; Chislov, M.; Baas, J.; Blake, G. R. Polar Structure and Two-Dimensional Heisenberg Antiferromagnetic Properties of Arylamine-Based Manganese Chloride Layered Organic–Inorganic Perovskites. *Inorg. Chem.* **2021**, *60*, 15151–15158; (b) Lee, K. W.; Lee, C. H.; Lee, C. E.; Kang, J. K. Magnetic Ordering in Two-Dimensional Heisenberg Antiferromagnets with Variable Interlayer Distances. *Phys. Rev. B* **2000**, *62*, 95–98.
[19] (a) Dolomanov, O. V.; Bourhis, L. J.; Gildea, R. J.; Howard, J. A. K.; Puschmann, H. Olex2: A Complete Structure Solution, Refinement and Analysis Program. *J. Appl. Crystallogr.* **2009**, *42*, 339–341; (b) Sheldrick, G. M. SHELXY - Integrated Space-Group and Crystal-Structure Determination. *Acta Crystallogr. A*: *Found. Adv.* **2015**, *71*, 3–8.

Manuscript received: June 2, 2025
Manuscript revised: July 15, 2025
Manuscript accepted: July 17, 2025
Version of record online: August 12, 2025

The Authors

Left to Right: Sinuo Li, Richard J. Harrison, Wei Li, Michael A. Carpenter

